The Journal of Chemical Physics

RESEARCH ARTICLE | FEBRUARY 27 2020

Substituent effects on nonadiabatic excited state dynamics: Inertial, steric, and electronic effects in methylated butadienes

Special Collection: Ultrafast molecular sciences by femtosecond photons and electrons

Ryan J. MacDonell; María E. Corrales; Andrey E. Boguslavskiy; Luis Bañares ; Albert Stolow; Michael S. Schuurman

J. Chem. Phys. 152, 084308 (2020)
https://doi.org/10.1063/1.5139446

The Journal of Chemical Physics ARTICLE scitation.org/journal/jcp

Substituent effects on nonadiabatic excited state dynamics: Inertial, steric, and electronic effects in methylated butadienes

Cite as: J. Chem. Phys. 152, 084308 (2020); doi: 10.1063/1.5139446
Submitted: 19 November 2019 • Accepted: 6 February 2020 •
Published Online: 27 February 2020

Ryan J. MacDonell,[1] María E. Corrales,[2] Andrey E. Boguslavskiy,[3] Luis Bañares,[2] Albert Stolow,[1,3,4,a)] and Michael S. Schuurman[1,4,b)]

AFFILIATIONS

[1]Department of Chemistry and Biomolecular Sciences, University of Ottawa, Ottawa, Ontario K1N 6N5, Canada
[2]Departamento de Química Física, Facultad de Ciencias Químicas, Universidad Complutense de Madrid, 28040 Madrid, Spain
[3]Department of Physics, University of Ottawa, Ottawa, Ontario K1N 6N5, Canada
[4]National Research Council of Canada, 100 Sussex Drive, Ottawa, Ontario K1A 0R6, Canada

Note: This paper is part of the JCP Special Topic on Ultrafast Molecular Sciences by Femtosecond Photons and Electrons.
[a)]**E-mail:** astolow@uottawa.ca
[b)]**Author to whom correspondence should be addressed:** michael.schuurman@nrc-cnrc.gc.ca

ABSTRACT

The photochemical dynamics of double-bond-containing hydrocarbons is exemplified by the smallest alkenes, ethylene and butadiene. Chemical substituents can alter both decay timescales and photoproducts through a combination of inertial effects due to substituent mass, steric effects due to substituent size, and electronic (or potential) effects due to perturbative changes to the electronic potential energy surface. Here, we demonstrate the interplay of different substituent effects on 1,3-butadiene and its methylated derivatives using a combination of *ab initio* simulation of nonadiabatic dynamics and time-resolved photoelectron spectroscopy. The purely inertial effects of methyl substitution are simulated through the use of mass 15 "heavy-hydrogen" atoms. As expected from both inertial and electronic influences, the excited-state dynamics is dominated by pyramidalization at the unsubstituted carbon sites. Although the electronic effects of methyl group substitution are weak, they alter both decay timescales and branching ratios by influencing the initial path taken by the excited wavepacket following photoexcitation.

I. INTRODUCTION

Conjugated polyenes play an important role throughout chemistry. In organic photochemistry, they are known for their low-lying bright electronic states, typically dominated by $\pi\pi^*$ excitations. Certain polyenes, particularly short-chain or polar polyenes, decay nonradiatively from an electronically excited state by passage through conical intersections between the ground and excited states. Many of these decay pathways are dominated by a single geometric motif: a 90° twist about a C=C bond followed by pyramidalization at one of the carbon atoms of the twisted bond. Passage through the conical intersection may result in isomerization about the twisted bond. This motion is characteristic of the excited-state dynamics of ethylene but also occurs in molecules as large as the retinal Schiff base chromophore in rhodopsin, responsible for initiating the vision signal in many organisms.[1–4] The localization of dynamics to a single carbon–carbon bond is potentially useful in areas of synthesis, light-harvesting, and photochemical switching.

The shortest polyene, 1,3-butadiene, serves as a model system for the dynamics of larger polyenes because it exhibits the dynamical aspects of both ethylene and longer polyenes. Conjugated polyenes typically have a low-lying, spectroscopically dark $(\pi^*)^2$ state and a bright $\pi\pi^*$ state at higher energy. In butadiene, these two states are nearly degenerate,[5,6] with the dark state roughly 0.2 eV lower in energy than the bright state.[7] The complexity of its UV absorption spectrum,[8,9] in conjunction with its small size,

has made butadiene a common benchmark for theoretical[7,10–19] and experimental[20–25] spectroscopic studies. The spectrum consists of a series of broad peaks ranging from 216 nm to 200 nm. Using reduced-dimensional linear vibronic coupling models, the form of the absorption spectrum was attributed to excitation to the bright $\pi\pi^*$ state, with initial motion along bond alternation of the carbon backbone and much of the coupling to the dark state due to out-of-plane C=C torsional modes.[15,16] A new paradigm was introduced by Levine and Martínez,[14] wherein both ethylenic and transoid dynamics participated and were in competition. Recently, further corrections to this model revealed a sensitivity of the spectrum to the coupling between excited states, with an additional dependence of the third absorption band due to coupling to a low-lying Rydberg state.[19]

The ultrafast electronic de-excitation of butadiene involves conical intersections of polarized electronic character (i.e., ionic pathways similar to the twist-pyramidalization of ethyene with a lone-pair configuration) and nonpolar character (i.e., covalent pathways related to the bond-alternation pathway, transoid and cisoid, with a tetraradical configuration). Recently, the $\pi\pi^*$ excited-state dynamics of butadiene were studied in detail using a combination of time-resolved photoelectron–photoion coincidence spectroscopy (TRPEPICO) and *ab initio* simulation,[18,25] largely corroborating the Levine and Martínez model.[14] Multi-state complete active space second-order perturbation theory (MS-CASPT2) calculations revealed that the C1 pyramidalization and transoid minimum energy conical intersections (MECIs) occur at nearly the same energies, and thus, both contribute to the excited state decay. *Ab initio* multiple spawning (AIMS) simulations revealed that the dynamics were largely dictated by the initial geometry, with a slightly greater proportion of the excited-state wavepacket passing through the transoid conical intersection region. By systematically varying the electronic structure method so as to favor either the $\pi\pi^*$ or $(\pi^*)^2$ states, the dynamics accordingly shifted to either ethylenic or transoid S_1–S_0 intersections.[18] Using TRPEPICO, the excited-state dynamics were characterized in detail, revealing the interplay of the two dynamical pathways. The extreme width of the UV absorption spectrum was also explained in terms of the rapid torsion about a C=C double bond.[25]

In a systematic but phenomenological approach to dynamics at conical intersections, we have focused on the effects of methylation on the nonadiabatic dynamics of small organic molecules.[26] In ethylene, increasing methylation stabilizes Rydberg-type states relative to the $\pi\pi^*$ valence state, slowing the Rydberg-to-valence dynamics considerably. In substituted ethylenes such as acrolein and acrylonitrile, methylation has a strong inertial effect on the dynamics, depending on the methylated position in the molecule.[27,28] For crotonaldehyde, in particular, methylation dramatically increases the decay timescale by decreasing the probability of internal conversion to the ground state, thereby increasing the probability of intersystem crossing from the $n\pi^*$ state.[28] Similarly, methylation of allene leads to the gradual dominance of the twist-bend (central carbon) as opposed to the twist-pyramidalized (terminal carbons) conical intersection, as explained by steric repulsion and slower vibrational frequencies due to the inertial effects of methylation.[29] A more dramatic effect was seen for adenine, where methyl substitution destabilizes a $\pi\sigma^*$ state, thus altering the dynamics by removing a decay pathway.[30,31] Many of these studies assumed that methyl group substitution introduces primarily an inertial effect, decreasing the velocity of the wavepacket along certain directions in coordinate space. The methyl substitution technique thus provides an approach for influencing how the nuclear wavefunction evolves as it passes through a region of strong nonadiabatic coupling.

Recently, it was shown that concepts of electron resonance for displacing electron density within molecules are also relevant for excited states. The dominant decay pathway of ethylene, twist-pyramidalization, occurs with a concurrent increase in charge density at the pyramidalized carbon. By adding a π-accepting CN group to ethylene[27] and butadiene,[32] it was shown that the potential energy surface is "tilted" to favor pyramidalization at the CN-substituted carbon. This effect dominates dynamics even in cases where pyramidalization at the substituted carbon is dynamically disfavored due to massive substituents.[27] The shift of MECI energies (and, thus, the shift of the potential energy surfaces) can be tuned by the choice of functional group. Finally, dynamical simulations of vinylamine (NH_2-substituted ethylene) showed how π-donors have the opposite effect, i.e., the dominant decay pathway is pyramidalization at the neighboring carbon site.[33]

The observed effects of substituents on nonadiabatic dynamics can be separated into three categories: inertial, steric, and electronic (or potential). Inertial effects result from changes in the mass of substituents and thus can be thought of as purely dynamical in nature,[34,35] whereas steric and electronic effects result in changes to the potential energy surfaces. In reality, any functional group substituent will lead to a combination of all three effects, the relative magnitudes of which depend on the mass, geometry, and electronic nature of the substituent. With the exception of the slight effects of isotopic substitution, disentangling these effects is difficult in real molecules; however, atomic masses can be readily varied in theoretical simulations. By introducing a "heavy-hydrogen" atom having the same mass as a chemical substituent, it is possible to characterize the purely inertial effects on the dynamics without concomitant changes to the underlying potential energy surface.

Although the methyl group was largely considered to be an "electronically inert" substituent in the past, it is a weak π-donor and should lead to some observable change in potential energy surfaces and associated gradients in the methylated molecule. For example, closer inspection of MECI energies of methylated acrylonitrile show 0.3 eV shifts, small relative to the 1 eV shift due to CN substitution.[27] Here, we study the effects of methyl substitution on the excited-state dynamics of 1,3-butadiene (BD). Specifically, we used symmetrically methylated derivatives of BD, 2,3-dimethyl-1,3-butadiene (central-dimethylbutadiene, C-MeBD) and 2,5-dimethyl-2,4-hexadiene (terminal-tetramethylbutadiene, T-MeBD), studied by a combination of time-resolved photoelectron spectroscopy (TRPES) and *ab initio* multiple spawning (AIMS) simulations. In the AIMS calculations, we replaced methyl substituents with hydrogen atoms of mass 15 u, yielding 2,3-$^{15}H_2$-1,3-butadiene ($^{15}H_2$-BD) and 1,1,4,4-$^{15}H_4$-1,3-butadiene ($^{15}H_4$-BD), the analogs of C-MeBD and T-MeBD, respectively. The structures of these molecules are shown in Fig. 1. By comparing the excited-state dynamics seen in the TRPES data to those calculated for the methylated species and the heavy-hydrogen atom species, we aim to isolate the role of the inertial effects on the nonadiabatic excited-state dynamics of 1,3-butadiene.

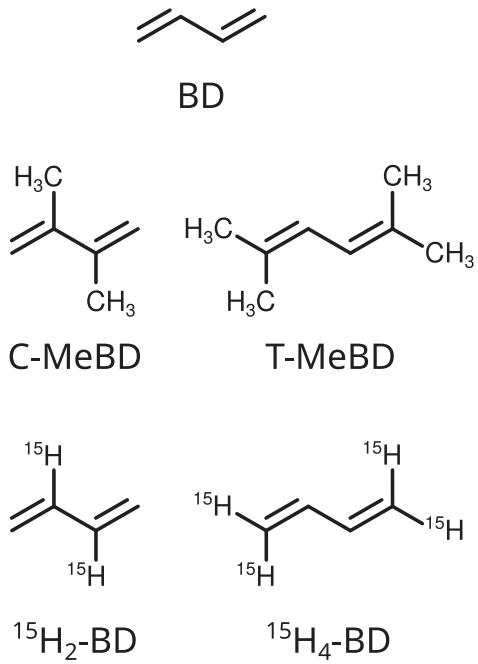

FIG. 1. Molecular structures of 1,3-butadiene (BD), 2,3-dimethyl-1,3-butadiene (C-MeBD), 2,5-dimethyl-2,4-hexadiene (T-MeBD), 2,3-$^{15}H_2$-1,3-butadiene ($^{15}H_2$-BD),and 1,1,4,4-$^{15}H_4$-1,3-butadiene ($^{15}H_4$-BD).

II. METHODS

A. Experimental methods

TRPES experiments[36] were performed using a magnetic bottle photoelectron spectrometer with a seeded pulsed molecular beam produced by an Even-Lavie 1 kHz pulsed valve. Chemicals for these experiments, 1,3-butadiene (BD, Matheson, 99.9%), 2,3-dimethyl-1,3-butadiene (C-MeBD, Alpha Aesar, 98%), and 2,5-dimethyl-2,4-hexadiene (T-MeBD, Alpha Aesar, 96%), were used without further purification. One femtosecond laser was tuned to 237.4 nm so as to be in resonance with the target T-MeBD $\pi\pi^*$ state. The other femtosecond laser was set to 200 nm. Thus, for BD and C-MeBD, the 200 nm pulse was the pump, whereas for T-MeBD, the 237 nm pulse was the pump. In all cases, the other fs laser pulse acted as the time-delayed probe, which, by single-photon ionization of the excited state, generated the photoelectron spectrum. Tuneable femtosecond UV laser pulses were produced via frequency mixing the output of a 35 fs, 800 nm, 1 kHz Ti:sapphire regenerative amplifier (Coherent Legend Elite). The 237.4 nm beam was generated with Light Conversion's TOPAS and its DUV Extension module pumped with 800 nm ($\nu_{pump} + 2(2\nu_{signal})$ nonlinear mixing scheme). The 200.4 nm is the 4th harmonic of the 800 nm. The resulting UV pulses were separated from the fundamental and intermediate frequency counterparts by three or more reflections off suitable dichroic mirrors. Both pump and probe pulses were compressed using VUV-grade CaF_2 prism pairs, thus managing dispersion in air and in the vacuum input window, and then combined co-linearly on a thin dichroic mirror. The combined pulses were focused by a deep UV aluminum (DUVA) coated concave spherical mirror (f = 0.5 m) into the interaction region of a magnetic bottle photoelectron spectrometer where they intercepted the pulsed seeded (alternatively 1% BD, 1% C-MeBD, or 0.1% T-MeBD in helium) molecular beam. The ensuing energy-resolved photoelectron spectrum, recorded as a function of time delay between pump and probe laser pulses (controlled by a motorized translation stage), thus yields the time-resolved photoelectron spectrum (TRPES). During the time delay scan, the beams were modulated with computer controlled shutters at every time delay and three measurements were taken: pump-probe, pump-only, and probe-only; the latter two were subtracted in all plots presented. Immediately before and after every experimental run, a short scan was used to register the nonresonant $[1 + 1']$ ionization of xenon, determining the time zero, t_0, and cross correlation width (instrument response function) later used in fits. Photoelectron kinetic energies were calibrated using the well-known one-color photoelectron spectrum of BD.

As in previous experiments,[25,27,37] the TRPES data were globally fit to a 2D surface of the form

$$S(E, \Delta t) = g(\Delta t) \otimes \sum_i D_i(E) \exp(-\Delta t/\tau_i), \quad (1)$$

where $g(\Delta t)$ is a Gaussian cross-correlation function and $D_i(E)$ is the ith time-independent, energy-resolved decay associated spectrum (DAS) correlated with time constant τ_i. Large-amplitude motion of the excited state wavepacket can give rise to a "chirp" in the photoelectron energies as a function of time, an effect that is not included in the DAS. Thus, to account for this, the time zero (t_0) of the exponential decay is included as a variable in the fit as a function of energy, yielding $\Delta t = t - t_0(E)$, where t is the experimental pump–probe time delay.[37] The measured full width at half maxima of the cross-correlation signal used in the fits were 95 fs, 104 fs, and 110 fs for BD, C-MeBD, and T-MeBD, respectively.

Electronic absorption spectra were measured for C-MeBD and T-MeBD in the vapor phase using a Varian Cary 5000 UV–Vis–NIR spectrophotometer, shown in Fig. 2. The UV spectrum of BD is also given for comparison.[8] The broad features around 200–230 nm and 220–250 nm for C-MeBD and T-MeBD, respectively, are assigned to the bright $\pi\pi^*$ absorption band characteristic of alkenes.

B. Computational methods

Critical points on the potential energy surfaces of BD, C-MeBD, and T-MeBD were characterized by optimizing structures using single-excitation multireference configuration interaction (MR-CIS) with a 6-31G* basis and a four electron, four orbital active space for all molecules. State averaging was performed over the three lowest-lying states of the multiconfigurational self-consistent field reference. Ground- and excited-state potential energies were calculated at the MR-CIS/6-31G* level of theory and compared to multi-state complete active space second-order perturbation theory (MS-CASPT2) with a cc-pVTZ basis, as shown in Figs. S7 and S8 of the supplementary material. MR-CIS calculations were performed with the COLUMBUS software package,[38] while MS-CASPT2 calculations were performed using Molcas.[39,40]

The MR-CIS calculations showed good agreement with the trends in MS-CASPT2 energies, and thus, the MR-CIS/6-31G* level of theory was employed for nonadiabatic molecular dynamics using

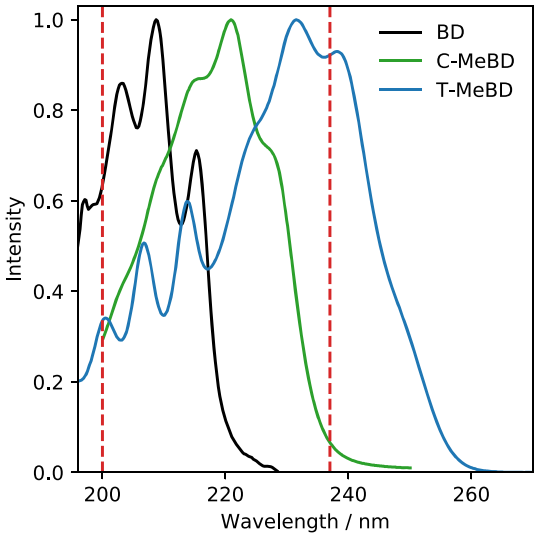

FIG. 2. Experimental absorption spectra of BD, C-MeBD, and T-MeBD. Vertical dashed lines show the pump and probe wavelengths. The BD spectrum is reprinted with permission from Leopold *et al.*, J. Chem. Phys. **81**, 4218–4229 (1984). Copyright 1984 AIP Publishing.

the *ab initio* multiple spawning (AIMS) formalism.[41–43] The molecular wavefunction was expanded over electronic states ψ and nuclear basis functions χ as

$$\Psi(\mathbf{r},\mathbf{R},t) = \sum_{I=1}^{N_s}\sum_{j=1}^{N_I(t)} c_j^I(t)\psi_j^I(\mathbf{r},\mathbf{R})\chi_j^I(\mathbf{R},t). \quad (2)$$

The total number of electronic states, N_s, is three: the ground, $\pi\pi^*$, and $(\pi^*)^2$ states. The number of nuclear basis functions on state I, $N_I(t)$, was changed over time by spawning a new basis function to a coupled state when the coupling exceeded a given threshold. The nuclear basis was composed of frozen-width Gaussian functions with time-dependent, classically evolving positions, momenta, and phases. Expansion coefficients c_j^I were found for each time step using the time-dependent Schrödinger equation. Initial conditions were sampled from a $v = 0$ vibrational distribution obtained from Hessians calculated at the RI-MP2/cc-pVDZ level of theory using Turbomole.[44,45] The initial position and momentum of the C-MeBD and T-MeBD trajectories were resampled until the initial trajectory was within 150 cm^{-1} of the pump energy plus a correction relative to MS-CASPT2 (6.20 + 0.78 eV for C-MeBD and 5.23 + 0.97 eV for T-MeBD). Each initial condition was treated as a separate simulation according to the independent first-generation approximation.[46] Thus, 40 and 36 initial conditions led to 521 and 702 trajectories over the course of the simulation for C-MeBD and T-MeBD, respectively.

Separate calculations were performed to simulate only inertial effects by artificially changing certain hydrogen-atom masses to the total mass of a methyl group (15.0234 u). The heavy-hydrogen atoms were selected to correspond to methylation of central ($^{15}H_2$-BD) and terminal ($^{15}H_4$-BD) carbons. The Hessian and the nuclear Gaussian widths were appropriately scaled for the change in mass. Excitation was assumed to be vertical, i.e., without the additional pump selection criteria for initial conditions, since there was not a corresponding experiment for the heavy-hydrogen species. As a result of the different initial condition criteria, the initial conditions of methylated species were more tightly distributed along certain vibrational modes relative to the heavy-hydrogen molecules, as shown in Figs. S2–S4 of the supplementary material. 40 initial conditions for both systems resulted in 622 and 565 trajectories for $^{15}H_2$-BD and $^{15}H_4$-BD, respectively. Comparisons to unsubstituted BD were done using data from previous published work.[32]

Time-resolved photoelectron spectra were simulated to facilitate direct comparison to experiment. Using the wavefunction expansion given in Eq. (2), the photoelectron signal is given by[27,47,48]

$$S(E,t) = \sum_{I=1}^{N_s^0}\sum_{j=1}^{N_I(t)} \left|c_j^I(t)\right|^2 \sum_{J=1}^{N_s^+}\sum_{n=1}^{2} w_j^{IJ}(n,t)\delta\left(E - \left[n\omega - \Delta E_j^{IJ}(t)\right]\right), \quad (3)$$

$$w_j^{IJ}(n,t) = \begin{cases} \left|\phi_j^{IJ}(t)\right|^2, & n = 1 \\ 0.01, & n = 2, \end{cases} \quad (4)$$

where labels 0 and + signify neutral and cation states, $\phi_j^{IJ}(t)$ is the Dyson orbital norm[49] between neutral state I and cation state J of trajectory j at time t, and likewise $\Delta E_j^{IJ}(t)$ is the ionization potential for the same states, trajectory, and time. The probe energy is given by $n\omega$, where n is the probe photon count. Based on previous work,[27] Dyson orbital weighting was only used for one-photon signals. A two-photon signal weighted by a factor of 0.01 was used for the unsubstituted BD spectrum only. After generating $S(E, t)$, the final spectrum was calculated by convolution with Gaussian functions along both axes. All spectra used an energy width of $\sigma_E = 0.1$ eV and time widths of σ_t = 35.25 fs, 38.22 fs, and 44.16 fs for BD, C-MeBD and T-MeBD, respectively, to agree with experimental parameters.

Iterative Hirshfeld charges were used to characterize the electronic structure of molecules in conical intersection regions by evaluating electronic densities on a molecular grid and finding the difference with spherically averaged atomic densities.[50,51] In previous work, we have shown that local differences in partial atomic charges and nuclear geometry give a robust separation of different portions of the seam space of small polyenes.[32,33]

III. RESULTS AND DISCUSSION

In Fig. 2, we show the gas phase UV absorption spectra of BD,[8] C-MeBD, and T-MeBD. The dashed red vertical lines indicate the fs laser wavelengths used here. For T-MeBD, the 237 nm pulse acted as the pump, whereas for BD and C-MeBD the 200 nm pulse acted as the pump. Although neither BD nor C-MeBD absorb at 237 nm, there is some non-zero absorption by T-MeBD at 200 nm. Therefore, the TRPES data for T-MeBD can contain both pump–probe and probe–pump photoelectron spectra. These overlap only at the time-zero point and can be treated by fitting the data in both positive (pump–probe) and negative (probe–pump) time delay directions.

The MR-CIS/6-31G* potential energies of critical points on the potential energy surfaces of BD, C-MeBD, and T-MeBD are shown in Fig. 3, with the symbol ⧖ used to indicate MECI geometries. In comparison with our previous study of a cyano substituent (a strong π-acceptor),[32] the energy shifts caused by methyl substitution are relatively small. At the optimized ground-state minimum

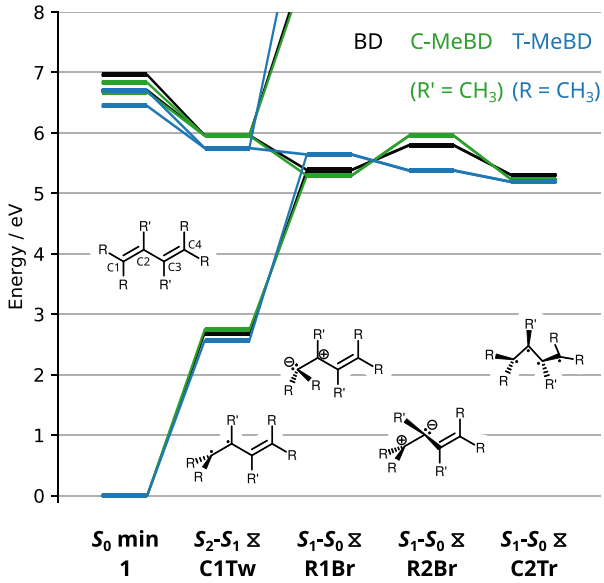

FIG. 3. Potential energies of critical points for BD (black), C-MeBD (green), and T-MeBD (blue), relative to their respective ground-state minimum energy, optimized and calculated at the MR-CIS/6-31G* level of theory. The carbon backbone numbering and the structures of the S_2–S_1 and S_1–S_0 MECIs are also shown.

(**1**), methylation led to slight differences in excited-state characters. Unsubstituted BD is known to have nearly degenerate $\pi\pi^*$ and $(\pi^*)^2$ states, and the $(\pi^*)^2$ state is lower in energy (S_1) than the $\pi\pi^*$ state (S_2) at higher levels of theory.[10,14,18] Here, the MR-CIS energies of BD follow the same trend. C-MeBD follows the same state ordering as unsubstituted BD, whereas the $\pi\pi^*$ state of T-MeBD is lower in energy (S_1); however, for all three molecules, the near degeneracy of the two states means that the state ordering can swap with small changes in geometry.

The energy of the S_2–S_1 C1C2-twist MECI (**C1Tw**) of C-MeBD (relative to the ground-state minimum) is the same as that of unsubstituted BD, while the T-MeBD **C1Tw** energy is decreased by less than 0.3 eV. For the S_1–S_0 transition, C-MeBD exhibits a decrease in the **R1Br** MECI (pyramidalization/bridging of the C1 substituent, i.e., H or CH_3) energy and an increase in the **R2Br** MECI (pyramidalization/bridging of the C2 substituent) energy of ~0.2 eV, while a more pronounced 0.4–0.5 eV shift occurs for T-MeBD. The **R1Br** geometry of T-MeBD appears to be sterically hindered due to the two methyl groups on the pyramidalized carbon atom, leading to C—CH_3 bond lengths of 1.7–1.8 Å. All of the S_1–S_0 MECI energies match the expectations of chemical intuition based on the weak π-donor characteristic of methyl groups. Notably, the energy of the **C2Tr** MECI (kinked-diene/transoid) decreases with increasing number of substituents, consistent with the independence of substituent position previously seen for cyanobutadienes.[32]

In Figs. 4(a)–4(c), we show the experimental TRPES data for all three molecules, with the positive time representing the delay between pump and probe pulses. All spectra show a spectral shift from higher to lower kinetic energies with increasing time delay, particularly for T-MeBD with the largest observed shift. The T-MeBD spectrum also exhibits a long-lived band from 0 eV to 2.2 eV, which does not appear in the other spectra. The simulated spectra are shown in Figs. 4(d)–4(f) and are described and compared to the experimental results below.

The calculated initial adiabatic populations of C-MeBD and T-MeBD are shown in Figs. 5(a) and 5(b). The initial conditions were selected based on the experimental pump photon energies and the strength of the electronic transition dipole, resulting in 65% and 43% of the initial population on S_2 for C-MeBD and T-MeBD,

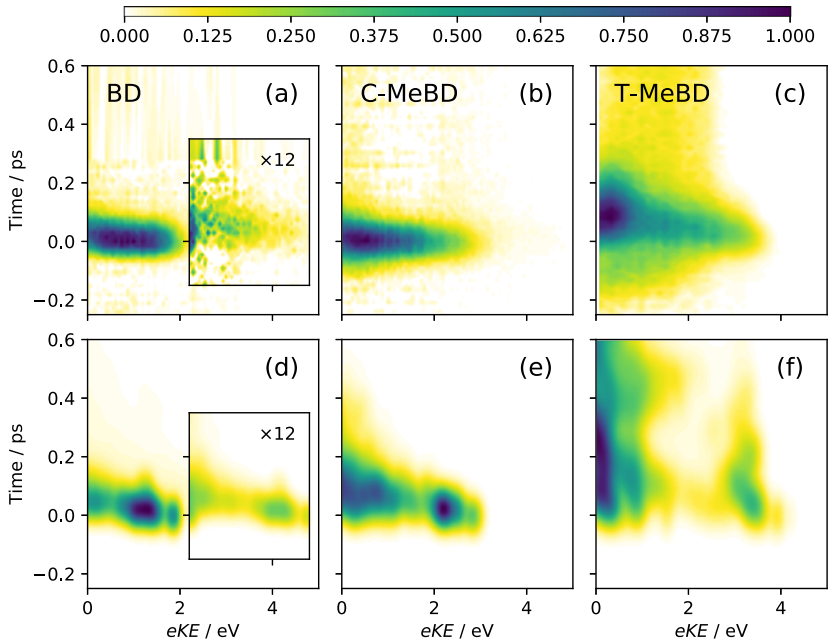

FIG. 4. Experimental [(a)–(c)] and theoretical [(d)–(f)] normalized TRPES of BD, C-MeBD, and T-MeBD (from left to right, respectively) as a function of electron kinetic energy and pump–probe delay. Insets of (a) and (d) are scaled signals due to absorption of two probe photons (producing higher kinetic energy photoelectrons) displayed on the same axes as the unscaled spectra.

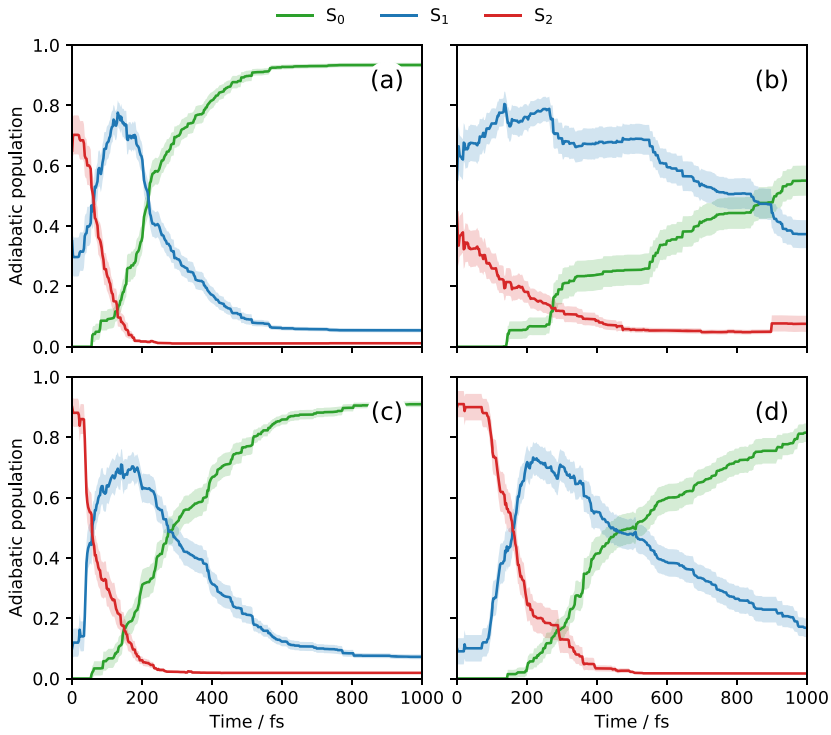

FIG. 5. Adiabatic populations of (a) C-MeBD, (b) T-MeBD, (c) $^{15}H_2$-BD, and (d) $^{15}H_4$-BD as a function of time. Shaded regions show one bootstrap standard deviation from the mean.

respectively. Also shown in Fig. 5 are the AIMS adiabatic populations as a function of time for C-MeBD and T-MeBD, as well as for the heavy-hydrogen species, $^{15}H_2$-BD and $^{15}H_4$-BD [Figs. 5(c) and 5(d)]. The initial populations of the heavy-hydrogen molecules are in good agreement with each other, as expected because the sampled potential surfaces are the same. The population curves show consistent sequential $S_2 \rightarrow S_1 \rightarrow S_0$ population dynamics with fast initial decay from S_2 and slower decay from S_1. The populations were fit to a first-order kinetic model of the form

$$S_2 \underset{\tau_{-1}}{\overset{\tau_1}{\rightleftharpoons}} S_1 \underset{\tau_{-2}}{\overset{\tau_2}{\rightleftharpoons}} S_0. \tag{5}$$

An initial time delay t_0 was also included. The equations for the populations of each state depend on t_0, the initial S_2 population $p_2(0)$ [assuming $p_1(0) = 1 - p_2(0)$], the forward decay constants τ_1 and τ_2, and the backward decay constants τ_{-1} and τ_{-2}. The full equations for populations as a function of time are given in Sec. 1 of the supplementary material. Note that the backward decay constants are important for obtaining fits when small populations remain on the excited states and do not necessarily represent the rate of population transfer from lower-energy to higher-energy states.

Fit values and their least-squares uncertainties for the populations in Fig. 5 are given in Table I. The fit τ_{-2} value of T-MeBD was many orders of magnitude larger than τ_2 and thus could be excluded with no significant changes in other values. The decay of C-MeBD is faster relative to $^{15}H_2$-BD, whereas for T-MeBD, the decay is slower than its heavy-hydrogen equivalent. The populations alone suggest a notable difference between the methyl-substituted vs the heavy-hydrogen substituted molecules. Part of this difference may result from differences in initial conditions. Figures S2–S4 show how the use of experimental pump energies for C-MeBD and T-MeBD led to tighter distributions along torsion, pyramidalization, and bond alternation modes relative to $^{15}H_2$-BD and $^{15}H_4$-BD. Sampling along the bond alternation mode, in particular, is shifted from

TABLE I. Time delays, initial populations, decay constants, and their least-squares uncertainties from fits to the adiabatic populations shown in Fig. 5.

Molecule	t_0 (fs)	$p_2(0)$	τ_1 (fs)	τ_{-1} (fs)	τ_2 (fs)	τ_{-2} (fs)
BD	52.2 ± 0.6	0.89 ± 0.01	22.6 ± 0.9	442 ± 25	240 ± 2	4 830 ± 120
C-MeBD	69.5 ± 2.1	0.62 ± 0.01	30.5 ± 3.1	2000 ± 1600	168.9 ± 3.3	3 590 ± 290
T-MeBD	89.2 ± 7.8	0.31 ± 0.01	111 ± 15	1130 ± 220	1301 ± 17	...
$^{15}H_2$-BD	47.1 ± 1.1	0.83 ± 0.01	41.9 ± 1.5	577 ± 33	234 ± 2	3 860 ± 100
$^{15}H_4$-BD	115.5 ± 1.3	0.88 ± 0.01	68.4 ± 1.8	1447 ± 69	455 ± 5	14 500 ± 3800

the ground state minimum, which may have the effect of a slight increase/decrease in the decay times of C-MeBD/T-MeBD, respectively, contrary to the observed changes in Table I. The increase in mass has a subtle effect on decay timescales, but the effect is greater for the methylated molecules, suggesting that the inertial (mass-weighting) effect does not fully account for the effects of methyl substitution. Comparing molecules, the S_2 decay (τ_1) is fastest for BD, followed by C-MeBD and the much slower T-MeBD. The S_1 decay (τ_2) is similarly slow for T-MeBD (1.30 ps), whereas the C-MeBD τ_2 decay is faster than that of BD by >70 fs. Interestingly, these results suggest faster excited-state decay dynamics for C-MeBD than for unsubstituted BD, despite the addition of heavy methyl groups.

In Figs. 4(d)–4(f), the energy shift seen in the experimental TRPES [Figs. 4(a)–4(c)] is reproduced but overestimated in the simulated spectra of all three molecules, particularly T-MeBD. This overestimation is consistent with past simulated spectra[18,27] and suggests an under-estimation of the excited state gradients relative to the gradients of the cation states. The experimental and theoretical data for BD and C-MeBD are otherwise in qualitative agreement. The BD spectra show similar features in the two-photon region (see the inset). The full BD spectra are in good agreement with recent results using a 216 nm pump and a 200 nm probe, as well as the corresponding simulated spectra.[18,25] In the theoretical spectrum of C-MeBD, there is a high-amplitude region around 2.2 eV, which comes from the $S_2 \rightarrow D_0$ transition. Excluding the Dyson-orbital norm weighting significantly reduces this intensity, suggesting that the ionization probability is over-estimated for that particular band. The $S_2 \rightarrow D_0$ band of T-MeBD appears as an oscillating feature around 3.5 eV. The spectrum without Dyson-orbital norms suggests a similar overestimation of the band intensity. For comparison, theoretical spectra without Dyson norm weighting factors are given in Fig. S6 of the supplementary material.

The theoretical TRPES of T-MeBD [Fig. 4(f)] shows significantly more structure than the experimental spectrum, with oscillations in the 1–2 eV range rather than the smooth evolution seen experimentally [Fig. 4(c)]. The oscillation continues with less intensity around 800 fs (shown in Fig. S6f of the supplementary material), suggesting some periodic motion of the excited-state wavepacket. Kinetic energies within that energy range result from $S_1 \rightarrow D_0$ transitions. The shift to lower energies (250 fs and 630 fs) coincides with pyramidalization at the central carbon in the vicinity of the **C2Tr** MECI for most trajectories, while the return to higher energies (440 fs and 820 fs) comes from a flattening around C2. The disagreement with experimental data may suggest that the low-frequency pyramidalization modes were under-sampled in the initial condition selection, leading to coherent motion in the theoretical spectrum that is "averaged out" in the experimental spectrum. Indeed, the pyramidalization mode had a particularly tight distribution for the initial conditions shown in Fig. S3 of the supplementary material. The long-lived plateau in the experimental spectrum includes photoelectron kinetic energies up to 2.2 eV. This is a significantly higher kinetic energy than one would expect for a hot ground-state spectrum, suggesting that a part of the wavepacket gets trapped on the excited state, in agreement with the theoretical results. The experimental T-MeBD spectrum also has observable dynamics in the negative time direction, which results from the absorption cross section at 200 nm being only somewhat smaller than that at 237 nm (see Fig. 2), and is not included in the simulation.

TABLE II. Decay constants for fits to the experimental and theoretical time-resolved photoelectron spectra. Errors correspond to the 90% confidence interval. See text for details.

	Experimental		Theoretical	
Molecule	τ_1 (fs)	τ_2 (fs)	τ_1 (fs)	τ_2 (fs)
BD	$7.8^{+1.9}_{-0.8}$	$13.8^{+4.2}_{-6.2}$	14.0 ± 2.1	$39.8^{+2.0}_{-4.0}$
C-MeBD	$8.0^{+2.8}_{-0.8}$	24^{+10}_{-15}	$40.9^{+8.2}_{-4.1}$	82.3 ± 8.2
T-MeBD	$24.8^{+9.9}_{-8.7}$	99^{+30}_{-20}	149^{+67}_{-45}	560^{+250}_{-220}

For the purpose of quantitative comparison between spectra, in Table II, we show global fits to the TRPES signal. The fit is based on the kinetic model $X \xrightarrow{h\nu} A \xrightarrow{\tau_1} B \xrightarrow{\tau_2} X$. Data errors were calculated by bootstrap sampling over experimental scans and theoretical initial conditions, which were then used as weights for χ^2 fitting. The bootstrap standard deviations are given in Fig. S5 of the supplementary material. To estimate the confidence interval of fitted parameters, each fitted parameter was fixed and systematically varied (with all other parameters relaxed in order to minimize χ^2) in increments of 5% of the parameter value until the obtained value of χ^2 reached the threshold for 90% confidence. This error analysis provides the maximum possible variation of a fitting parameter, which is consistent with a particular χ^2 range, as it takes into account multi-dimensional correlations that may exist between a given set of parameters. The error bars are thus asymmetric, reflecting the differences between increasing vs decreasing the values of fit constants. The experimental decay time constants are consistent with the observed trend in adiabatic populations, i.e., C-MeBD ≈ BD < T-MeBD. The first time constants (τ_1) of all three molecules are within the experimental cross correlation, whereas τ_2 is significantly longer for T-MeBD. The theoretical decay constants all overestimate the experimental results but follow a similar trend. There is a greater difference between C-MeBD and BD in the simulated spectra, and T-MeBD is nearly an order of magnitude greater than the experimental values. The qualitative differences between the simulated and experimental TRPES of T-MeBD likely originate in the propensity for the simulation to trap population on the excited state. This may arise due to an underestimation of the vertical excitation energy, which reduces the available amount of internal energy in the excited-state dynamics. Comparison of MS-CASPT2 energies in Fig. S8 of the supplementary material show a relatively large separation of S_2–S_1 MECI energies at the MR-CIS-optimized geometries, which indicates a poor description of the two excited states before they reach the S_1–S_0 conical intersection regions.

In Fig. 6, we show contour maps of the relaxed S_1 adiabatic surfaces as a function of pyramidalization angles of the terminal and central carbons, ϕ_{C1} and ϕ_{C2}, respectively. The $\phi_{C1} = \phi_{C2} = 0$ geometry corresponds to a 90° rotation of the C1—C2 bond and a slight torsion about the central C2—C3 bond, which is in the region of the S_2–S_1 MECI and thus represents a starting point for population on S_1. All points on the surfaces correspond to geometry optimizations with out-of-plane angles and C1—C2 and C3—C4 dihedral angles constrained. For reference, the **R1Br**, **R2Br**, and **C2Tr** MECI geometries are given by the red symbols ×, ⋆, and ∗, respectively. As previously noted, the BD surface [Figs. 6(c) and 6(d)] has nearly

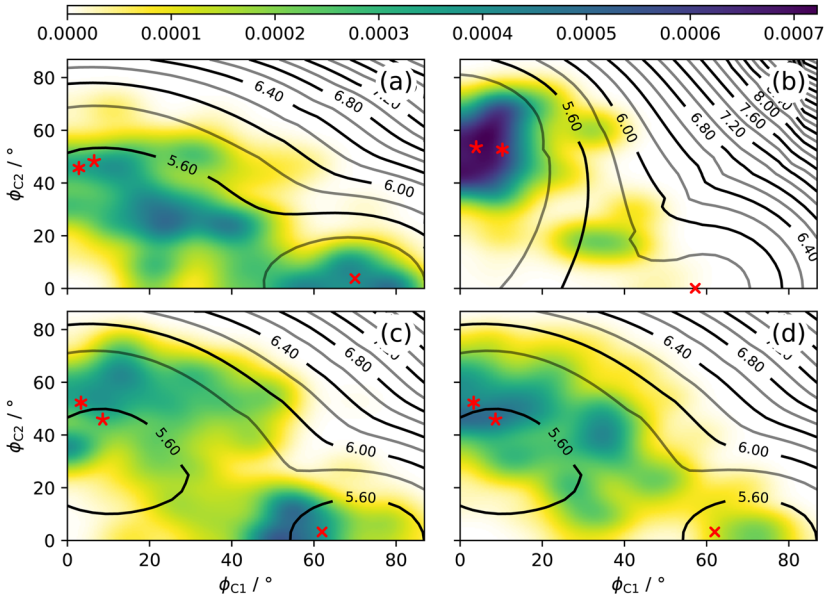

FIG. 6. Relaxed S_1 adiabatic surfaces (contours) and spawn populations (heatmap) as a function of pyramidalization angles of the terminal and central carbon atoms, ϕ_{C1} and ϕ_{C2}, for (a) C-MeBD, (b) T-MeBD, (c) $^{15}H_2$-BD, and (d) $^{15}H_4$-BD. The red symbols ×, ⋆, and ∗ represent **R1Br**, **R2Br**, and **C2Tr** MECIs, respectively.

degenerate potential energy wells along both pyramidalization coordinates with the initial gradient pointing toward C2 pyramidalization. The surfaces of C-MeBD and T-MeBD are only slightly shifted relative to previous results with cyano-substituted BD.[32] The potential energy well along ϕ_{C1} is lowered in energy for C-MeBD and increased in energy with a slight barrier in the case of T-MeBD.

Also shown as heatmaps in Fig. 6 are populations transferred during AIMS spawn events from the parent trajectory on S_1 to the child trajectory on S_0.[33] The S_1–S_0 population transfer is sufficiently localized around the spawn geometry to let us assume that the geometry is constant during population transfer. The heatmap of spawns is convoluted with a Gaussian of $\sigma = 5°$ along both pyramidalization angles. The spawn events show delocalization over the ϕ_{C1} and ϕ_{C2} wells for C-MeBD and the heavy-hydrogen molecules and localization of T-MeBD spawn populations along ϕ_{C2}. For the methylated species, the difference in spawn geometries can be explained by the changes in the potential energy surfaces. T-MeBD has a large energy barrier to C1 pyramidalization due to steric hindrance and π-donation from the two terminal methyl groups, whereas the **C2Tr** MECI remains energetically accessible for C-MeBD, thus leading to a greater range of geometries. In constrast, the heavy-hydrogen molecules have identical (electronic) potential energies, but there is

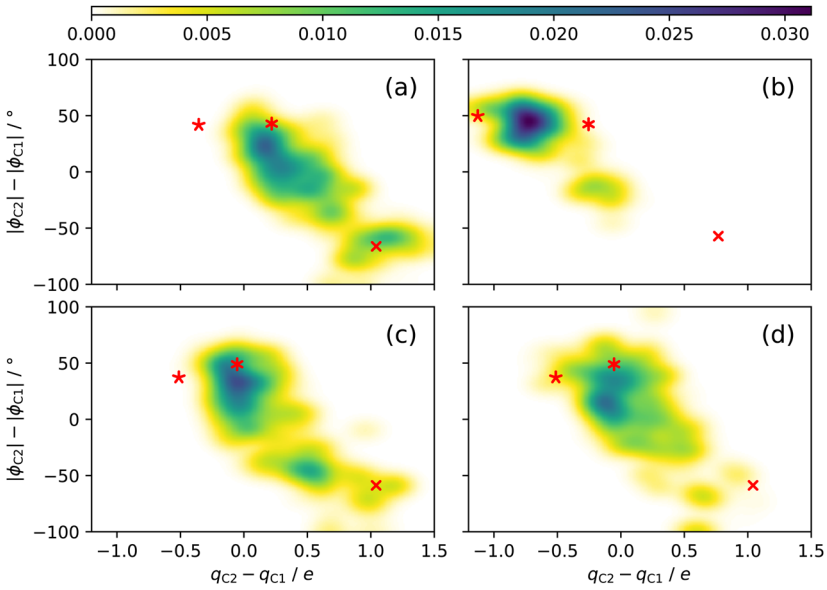

FIG. 7. S_1–S_0 spawn populations as a function of differences in charge and pyramidalization at C1 and C2 for (a) C-MeBD, (b) T-MeBD, (c) $^{15}H_2$-BD, and (d) $^{15}H_4$-BD. The red symbols ×, ⋆, and ∗ represent **R1Br**, **R2Br** and **C2Tr** MECIs, respectively.

still a notable difference in the spawn distributions. $^{15}H_4$-BD shows a decrease in C1 pyramidalization relative to $^{15}H_2$-BD. This difference is evidence of an inertial effect on the nonadiabatic dynamics in BD: with heavier terminal hydrogens, the C1 pyramidalization has a much lower frequency and the excited state wavepacket takes longer to access the **R1Br** conical intersection region.

Further characterization of the spawn geometries is given by analysis of the difference in electron density across the C1—C2 bond. In Fig. 7, we show the spawn populations as a function of partial atomic charge differences and pyramidalization differences at C1 and C2, with relevant MECIs given by red symbols as before. This analysis has previously been shown to give a good separation of electronic and nuclear characters into different regions of the conical intersection seam.[32,33] As before, T-MeBD shows the greatest localization with the majority of spawns occurring between **R2Br** and **C2Tr** geometries, i.e., with some transfer of electron density from C1 to C2. The spawns for the other systems have most population transfer occurring near **C2Tr**. The amount of **R1Br** population increases from $^{15}H_4$-BD to $^{15}H_2$-BD due to the inertial effect on the nonadiabatic dynamics and then from $^{15}H_2$-BD to C-MeBD due to the electronic effect of CH_3 π-donation.

These results and previous results with substituted ethylenes[33] and cyano-substituted butadienes[32] demonstrate the importance of electronic substituent effects (i.e., perturbations to the potential energy surface) on the nonadiabatic dynamics of small organic molecules, particularly polyenes. For strongly interacting substituents such as CN, the potential energies of MECIs may be shifted by more than 1 eV, leading to preference and inhibition of predictable low-frequency motions; however, even small changes due to a weak π-donor such as CH_3 lead to significant differences in wavepacket motion in comparison to unsubstituted BD. Steric repulsion from neighboring CH_3 groups can further tilt the potential energy surface, as seen in the case of T-MeBD. For both methylated butadienes, the change in decay timescales with respect to BD was underestimated by simulations that implemented heavy-hydrogen atoms at the appropriate positions. The nuclear and electronic character of spawn events for the heavy-hydrogen species closely resembled that of BD, which suggests that the shape of the potential energy surface (both energies and gradients) is likely more important than the relative masses for predicting branching ratios of conical intersection mediated dynamics.

IV. CONCLUSIONS

We are interested in the use of systematic chemical substitution in order to study dynamics at conical intersections. The molecule 1,3-butadiene is a paradigmatic example due to the role it plays in bridging the gap between ethylene and larger polyenes. Here, we applied methyl substitution to the case of butadiene. The nonadiabatic dynamics of methylated butadienes show evidence of inertial, steric, and electronic effects on both theoretical and experimental decay time constants as well as on the predicted branching ratios for the substituted molecules. Adding methyl groups to butadiene leads only to small (0.2–0.4 eV) shifts in the energies of twist-pyramidalization MECIs. Despite this, the changes in decay time constants and branching ratios for pyramidalization MECIs are underestimated by inertial effects alone, as in the theoretical simulations for the heavy-hydrogen species $^{15}H_2$-BD and $^{15}H_4$-BD. Closer inspection reveals that transitions to the ground electronic state occur in the lower energy regions of the potential energy surface, despite the small differences in energy. This suggests that electronic (potential) effects on nonadiabatic dynamics are significant even for weak π-donor substituents: methyl substitution cannot be assumed to be purely inertial in nature.

Our findings further reinforce the importance of studying how perturbative changes in electronic structure, e.g., resonance in polyenes, can lead to predictable changes in photochemical dynamics. Such predictions may be applied to tailoring photochemical reactions into highly specific products, with potential applications in synthetic organic chemistry, or may be used to alter excited state properties and lifetimes in order to optimize artifical light harvesting, photovoltaics, and photoswitching materials. An understanding of "dynamics–function" relationships will be important in the rational design of such materials.

SUPPLEMENTARY MATERIAL

See the supplementary material for an analysis of the population kinetic model, the initial condition sampling, the Dyson orbital norms and TRPES errors, MR-CIS and MS-CASPT2 potential energy surfaces, and optimized MR-CIS critical geometries of all molecules.

ACKNOWLEDGMENT

R.J.M., A.S., and M.S.S. acknowledge financial support from the Natural Sciences and Engineering Research Council of Canada (NSERC). M.E.C. and L.B. acknowledge financial support from Spanish MCIU under Grant No. PGC2018-096444-B-I00.

REFERENCES

[1] G. Gröbner, I. J. Burnett, C. Glaubitz, G. Choi, A. J. Mason, and A. Watts, "Observations of light-induced structural changes of retinal within rhodopsin," Nature **405**, 810–813 (2000).
[2] D. Polli, P. Altoe, O. Weingart, K. M. Spillane, C. Manzoni, D. Brida, G. Tomasello, G. Orlandi, P. Kukura, R. A. Mathies, M. Garavelli, and G. Cerullo, "Conical intersection dynamics of the primary photoisomerization event in vision," Nature **467**, 440–443 (2010).
[3] C. Punwong, J. Owens, and T. J. Martínez, "Direct QM/MM excited-state dynamics of retinal protonated Schiff base in isolation and methanol solution," J. Phys. Chem. B **119**, 704–714 (2015).
[4] P. Nogly *et al.*, "Retinal isomerization in bacteriorhodopsin captured by a femtosecond x-ray laser," Science **361**, eaat0094 (2018).
[5] W. Fuß, Y. Haas, and S. Zilberg, "Twin states and conical intersections in linear polyenes," Chem. Phys. **259**, 273–295 (2000).
[6] M. Garavelli, "Computational organic photochemistry: Strategy, achievements and perspectives," Theor. Chem. Acc. **116**, 87–105 (2006).
[7] M. A. Watson and G. K.-L. Chan, "Excited states of butadiene to chemical accuracy: Reconciling theory and experiment," J. Chem. Theory Comput. **8**, 4013–4018 (2012).
[8] D. G. Leopold, R. D. Pendley, J. L. Roebber, R. J. Hemley, and V. Vaida, "Direct absorption spectroscopy of jet-cooled polyenes. II. The $1^1B_u^+ \leftarrow 1^1A_g^-$ transitions of butadienes and hexatrienes," J. Chem. Phys. **81**, 4218–4229 (1984).
[9] G. Orlandi, F. Zerbetto, and M. Z. Zgierski, "Theoretical analysis of spectra of short polyenes," Chem. Rev. **91**, 867–891 (1991).
[10] M. Olivucci, I. N. Ragazos, F. Bernardi, and M. A. Robb, "A conical intersection mechanism for the photochemistry of butadiene. A MC-SCF study," J. Am. Chem. Soc. **115**, 3710–3721 (1993).

[11]L. Serrano-Andrís, M. Merchán, I. Nebot-Gil, R. Lindh, and B. O. Roos, "Towards an accurate molecular orbital theory for excited states: Ethene, butadiene, and hexatriene," J. Chem. Phys. **98**, 3151–3162 (1993).
[12]J. D. Watts, S. R. Gwaltney, and R. J. Bartlett, "Coupled-cluster calculations of the excitation energies of ethylene, butadiene, and cyclopentadiene," J. Chem. Phys. **105**, 6979–6988 (1996).
[13]M. Dallos and H. Lischka, "A systematic theoretical investigation of the lowest valence- and Rydberg-excited singlet states of trans-butadiene. The character of the 1^1B_u (V) state revisited," Theor. Chem. Acc. **112**, 16–26 (2004).
[14]B. G. Levine and T. J. Martínez, "Ab initio multiple spawning dynamics of excited butadiene: Role of charge transfer," J. Phys. Chem. A **113**, 12815–12824 (2009).
[15]A. Komainda, B. Ostojić, and H. Köppel, "Ab initio quantum study of nonadiabatic S_1–S_2 photodynamics of *s-trans*-Butadiene," J. Chem. Phys. A **117**, 8782–8793 (2013).
[16]A. Komainda, D. Lefrancois, A. Dreuw, and H. Köppel, "Theoretical study of the initial non-radiative 1 $B_u \rightarrow 2\ A_g$ transition in the fluorescence quenching of s-trans-butadiene: Electronic structure methods and quantum dynamics," Chem. Phys. **482**, 27–38 (2017).
[17]A. D. Chien, A. A. Holmes, M. Otten, C. J. Umrigar, S. Sharma, and P. M. Zimmerman, "Excited states of methylene, polyenes, and ozone from heat-bath configuration interaction," J. Phys. Chem. A **122**, 2714–2722 (2018).
[18]W. J. Glover, T. Mori, M. S. Schuurman, A. E. Boguslavskiy, O. Schalk, A. Stolow, and T. J. Martínez, "Excited state non-adiabatic dynamics of the smallest polyene, trans 1,3-butadiene. II. *Ab initio* multiple spawning simulations," J. Chem. Phys. **148**, 164303 (2018).
[19]S. M. Rabidoux, R. J. Cave, and J. F. Stanton, "Nonadiabatic investigation of the electronic spectroscopy of trans-1,3-butadiene," J. Phys. Chem. A **123**, 3255–3271 (2019).
[20]L. J. Rothberg, D. P. Gerrity, and V. Vaida, "Electronic spectra of butadiene and its methyl derivatives: A multiphoton ionization study," J. Chem. Phys. **73**, 5508–5513 (1980).
[21]D. L. Phillips, M. Z. Zgierski, and A. B. Myers, "Resonance Raman excitation profiles of 1,3-butadiene in vapor and solution phases," J. Phys. Chem. **97**, 1800–1809 (1993).
[22]F. Assenmacher, M. Gutmann, G. Hohlneicher, V. Stert, and W. Radloff, "Ultrafast dynamics of the 1^1B_u-state of 1,3-butadiene after excitation at 204 nm," Phys. Chem. Chem. Phys. **3**, 2981–2982 (2001).
[23]W. Fuß, W. E. Schmid, and S. A. Trushin, "Ultrafast electronic relaxation of *s-trans*-butadiene," Chem. Phys. Lett. **342**, 91–98 (2001).
[24]P. Hockett, E. Ripani, A. Rytwinski, and A. Stolow, "Probing ultrafast dynamics with time-resolved multi-dimensional coincidence imaging: Butadiene," J. Mod. Opt. **60**, 1409–1425 (2013).
[25]A. E. Boguslavskiy, O. Schalk, N. Gador, W. J. Glover, T. Mori, T. Schultz, M. S. Schuurman, T. J. Martínez, and A. Stolow, "Excited state non-adiabatic dynamics of the smallest polyene, trans 1,3-butadiene. I. Time-resolved photoelectron-photoion coincidence spectroscopy," J. Chem. Phys. **148**, 164302 (2018).
[26]M. S. Schuurman and A. Stolow, "Dynamics at conical intersections," Annu. Rev. Phys. Chem. **69**, 427–450 (2018).
[27]R. J. MacDonell, O. Schalk, T. Geng, R. D. Thomas, R. Feifel, T. Hansson, and M. S. Schuurman, "Excited state dynamics of acrylonitrile: Substituent effects at conical intersections interrogated via time-resolved photoelectron spectroscopy and *ab initio* simulation," J. Chem. Phys. **145**, 114306 (2016).
[28]A. M. D. Lee, J. D. Coe, S. Ullrich, M.-L. Ho, S.-J. Lee, B.-M. Cheng, M. Z. Zgierski, I.-C. Chen, T. J. Martínez, and A. Stolow, "Substituent effects on dynamics at conical intersections: α, β-enones," J. Phys. Chem. A **111**, 11948–11960 (2007).
[29]S. P. Neville, Y. Wang, A. E. Boguslavskiy, A. Stolow, and M. S. Schuurman, "Substituent effects on dynamics at conical intersections: Allene and methyl allenes," J. Chem. Phys. **144**, 014305 (2016).
[30]H. Kang, B. Jung, and S. K. Kim, "Mechanism for ultrafast internal conversion of adenine," J. Chem. Phys. **118**, 6717–6719 (2003).
[31]H. Satzger, D. Townsend, M. Z. Zgierski, S. Patchkovskii, S. Ullrich, and A. Stolow, "Primary processes underlying the photostability of isolated DNA bases: Adenine," Proc. Natl. Acad. Sci. U. S. A. **103**, 10196–10201 (2006).
[32]R. J. MacDonell and M. S. Schuurman, "Site-selective isomerization of cyano-substituted butadienes: Chemical control of nonadiabatic dynamics," J. Phys. Chem. A **123**, 4693–4701 (2019).
[33]R. J. MacDonell and M. S. Schuurman, "Substituent effects on the nonadiabatic dynamics of ethylene: π-donors and π-acceptors," Chem. Phys. **515**, 360–368 (2018).
[34]M. E. Corrales, V. Loriot, G. Balerdi, J. González-Vázquez, R. de Nalda, L. Bañares, and A. H. Zewail, "Structural dynamics effects on the ultrafast chemical bond cleavage of a photodissociation reaction," Phys. Chem. Chem. Phys. **16**, 8812–8818 (2014).
[35]M. L. Murillo-Sánchez, S. M. Poullain, J. J. Bajo, M. E. Corrales, J. González-Vázquez, I. R. Solá, and L. Bañares, "Halogen-atom effect on the ultrafast photodissociation dynamics of the dihalomethanes CH_2ICl and CH_2BrI," Phys. Chem. Chem. Phys. **20**, 20766–20778 (2018).
[36]A. Stolow, A. E. Bragg, and D. M. Neumark, "Femtosecond time-resolved photoelectron spectroscopy," Chem. Rev. **104**, 1719–1758 (2004).
[37]O. Schalk, A. E. Boguslavskiy, A. Stolow, and M. S. Schuurman, "Through-bond interactions and the localization of excited-state dynamics," J. Am. Chem. Soc. **133**, 16451–16458 (2011).
[38]H. Lischka *et al.*, COLUMBUS, an *ab initio* electronic structure program, release 7.0, 2012.
[39]F. Aquilante *et al.*, "Molcas 8: New capabilities for multiconfigurational quantum chemical calculations across the periodic table," J. Comput. Chem. **37**, 506–541 (2016).
[40]S. Vancoillie, M. G. Delcey, R. Lindh, V. Vysotskiy, P. Malmqvist, and V. Veryazov, "Parallelization of a multiconfigurational perturbation theory," J. Comput. Chem. **34**, 1937–1948 (2013).
[41]T. J. Martínez, M. Ben-Nun, and R. D. Levine, "Multi-electronic-state molecular dynamics: A wave function approach with applications," J. Phys. Chem. **100**, 7884–7895 (1996).
[42]T. J. Martínez, M. Ben-Nun, and R. D. Levine, "Molecular collision dynamics on several electronic states," J. Phys. Chem. A **101**, 6389–6402 (1997).
[43]M. Ben-Nun, J. Quenneville, and T. J. Martínez, "Ab initio multiple spawning: Photochemistry from first principles quantum molecular dynamics," J. Phys. Chem. A **104**, 5161–5175 (2000).
[44]R. Ahlrichs, M. Bär, M. Häser, H. Horn, and C. Kölmel, "Electronic structure calculations on workstation computers: The program system turbomole," Chem. Phys. Lett. **162**, 165–169 (1989).
[45]F. Weigend and M. Häser, "RI-MP_2: First derivatives and global consistency," Theor. Chem. Acc. **97**, 331–340 (1997).
[46]M. D. Hack, A. M. Wensmann, D. G. Truhlar, M. Ben-Nun, and T. J. Martínez, "Comparison of full multiple spawning, trajectory surface hopping, and converged quantum mechanics for electronically nonadiabatic dynamics," J. Chem. Phys. **115**, 1172–1186 (2001).
[47]H. R. Hudock, B. G. Levine, A. L. Thompson, H. Satzger, D. Townsend, N. Gador, S. Ullrich, A. Stolow, and T. J. Martínez, "Ab initio molecular dynamics and time-resolved photoelectron spectroscopy of electronically excited uracil and thymine," J. Phys. Chem. A **111**, 8500–8508 (2007).
[48]H. R. Hudock and T. J. Martínez, "Excited-state dynamics of cytosine reveal multiple intrinsic subpicosecond pathways," ChemPhysChem **9**, 2486–2490 (2008).
[49]M. Spanner, S. Patchkovskii, C. Zhou, S. Matsika, M. Kotur, and T. C. Weinacht, "Dyson norms in the XUV and strong-field ionization of polyatomics: Cytosine and uracil," Phys. Rev. A **86**, 053406 (2012).
[50]F. L. Hirshfeld, "Bonded-atom fragments for describing molecular charge densities," Theor. Chim. Acta. **44**, 129–138 (1977).
[51]P. Bultinck, C. V. Alsenoy, P. W. Ayers, and R. Carbó-Dorca, "Critical analysis and extension of the Hirshfeld atoms in molecules," J. Chem. Phys. **126**, 144111 (2007).